TU Delft Delft University of Technology

Master Thesis

Neutron Radiography of supercritical fluids

Author:
J.D. Korpershoek

Supervisor:
Dr.ir. M. Rohde

Faculty of Applied Sciences
Reactor Physics and Nuclear Materials (RPNM)
November 8, 2021

Abstract

This thesis investigates the possibility of measuring the density profile of supercritical fluids with the use of neutron radiography. One of the generation IV nuclear reactors currently under investigation makes use of supercritical water. One of the challenges of this design is predicting the fluid flow of the supercritical water. Being able to measure the density profile of a supercritical fluid in an experimental setup could help to gain insight in the fluid flow and could be an extra tool to verify computational models.
A possible tool for this purpose is the use of neutron radiography. This is a 2D imaging tool, where the average macroscopic cross section in the direction of measurement can be detected by the change in neutron intensity. Because the macroscopic cross section is proportional to the density, the density field can theoretically be extracted from this result.
In this work neutron radiography is used to measure density profiles, mimicked by polyethylene slopes, and the restrictions and optimal settings for this technique are further investigated.
One of the most surprising results was the fact that for atoms with a high scatter cross section, like hydrogen, the scattered neutrons invoke a large error to the measurement. In this thesis a method is introduced and tested to remove this blur from the results. The most challenging part of this method is finding the right scatter angle distribution.
More research is necessary to gather insight in how to find the scatter angle distribution and it seems likely that with the correct distribution the density profile of super critical fluids can be measured with the use of neutron radiography.

Contents

1 Introduction

Supercritical water is widely used in the industry, since its high pressure and temperature give it some interesting properties. It is for these properties, the use of supercritical water is investigated in the nuclear energy field. A challenge in the design of a supercritical water reactor is calculating the buoyancy effects of supercritical water. Being able to measure the density field of supercritical water could help to validate designs and computermodels. Existing density measurement techniques are not very suited for measuring super critical water, since they make use of light rays and need transparent materials, something which is hard to achieve at the high pressures of supercritical water. High pressures are less of an issue for neutron radiography. This chapter will go into more detail about supercritial fluids, reactors, neutron radiography and existing measurement techniques, which form the motivation for the research question. In the last paragraph the outline of the rest of this thesis is given.

1.1 Supercritical fluids

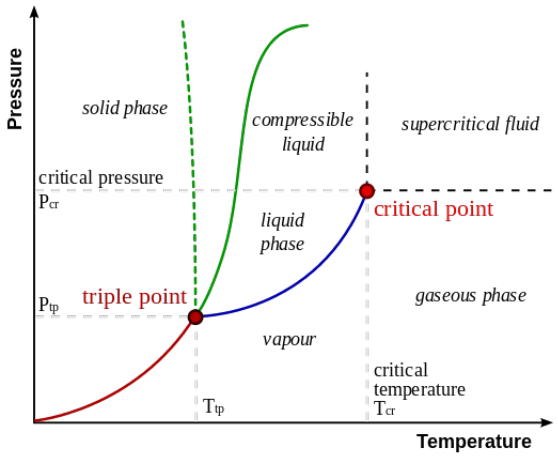

Figure 1: Phase diagram with pressure and temperature on the axis.

In a phase diagram, with on the axis the temperature and pressure, a line can be drawn between the liquid and gaseous phase, defining the boiling points for that particular fluid. At a certain temperature and pressure this line stops in the critical point. When the temperature and the pressure of a fluid both exceed their critical value that substance is per definition in a supercritical state. In the supercritical region there are no boiling points anymore and therefore a fluid can change from a fluid to a gas by going through the supercritical region without incurring a phase transition. The closer however to the critical point, the more abrupt the changes are. In figure 2 the density and specific heat are plotted as a function of temperature, for a pressure just above the critical

point. A sharp decrease of the density and a sharp peak for the specific heat can be observed. Increasing the pressure in this plot would result in a more gradual chance of these properties. Supercritical fluids are used as a working fluid in power plants, because the high temperature results in a better efficiency. Another application of supercritical fluids is the extraction of specific solvents. It is for example used in the decaffeinating of coffee beans.

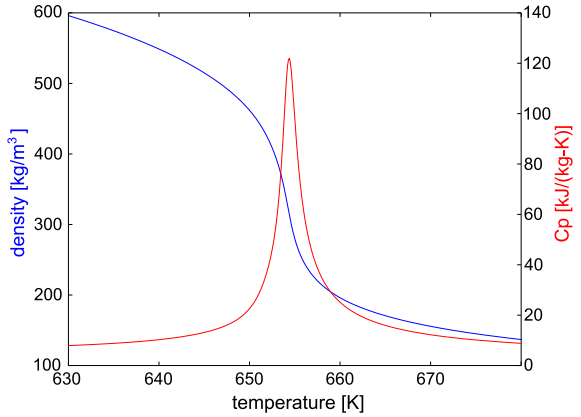

Figure 2: Density and specific heat profile for supercritical water a pressure of 24Mpa.

1.2 Supercritical water reactor

For nuclear energy there is a design in which supercritical water is being used. This is one of the generation-IV nuclear power plants and is abbreviated as SCWR: SuperCritical Water Reactor. The main advantage of using supercritical water is the higher efficiency. A SCWR has an expected efficiency of around 45%, while the current Light Water Reactors have an efficiency of around 33%. The SCWR is designed as a single-cycle system, meaning that the supercritical water is directly used to power a generator. This single-cycle is possible because the working fluid does not undergo a phase change, so no separation of phases is needed. A challenge for designing a SCWR is that still a lot is unknown about how to calculate the fluid-flow of supercritical fluids [2]. Big density changes have a major influence on fluid flows, heat transfer and moderation of fast neutrons. At the Reactor Physic and Nuclear Materials group, RPNM, research is being done on computer models that predict the fluid flow of supercritical fluids, both by improving these models and validation with measurements of supercritical flows. The measurement technique introduced in this research could also be used to validate computational models.

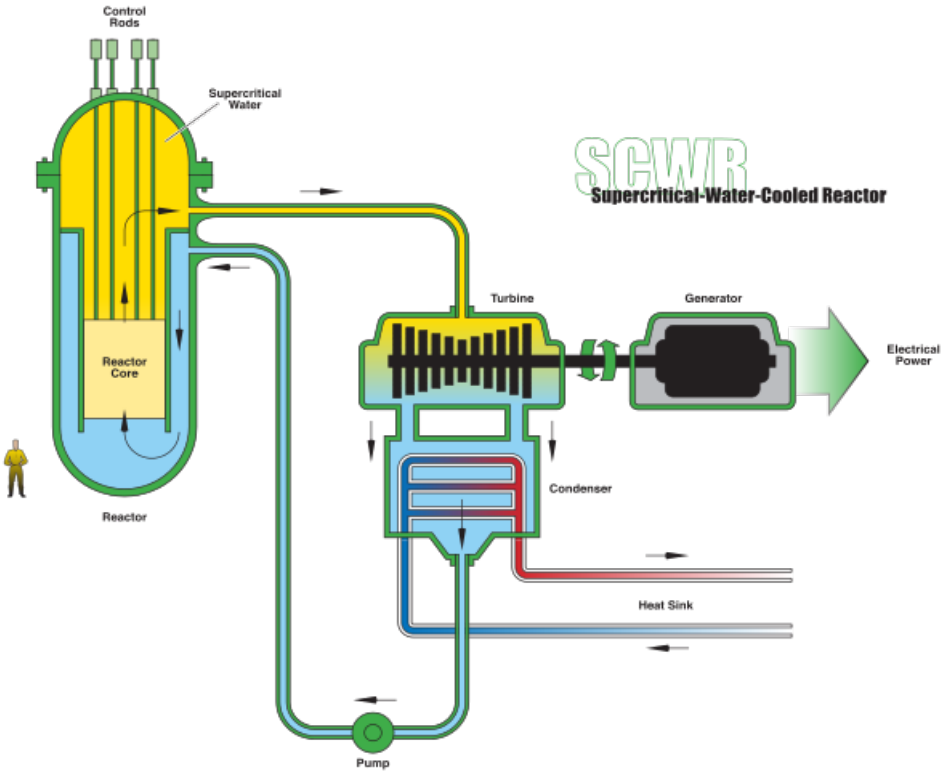

Figure 3: Scheme of a supercritical water reactor.

1.3 Neutron radiography

Neutron Radiography is an imaging technique where the interaction between a sample and neutrons can be measured. Since neutrons don‘t interact with electric charge, unlike X-rays, they can give a completely different contrast on an image[3]. The basic principle of neutron radiography is that you can measure the difference in absorption or scattering of neutrons by different materials, by putting your sample in a neutron bundle and detecting the drop in intensity. Strong neutron absorbers are for example hydrogen and gadolinium, and weak neutron absorbers are for example lead and aluminium. This makes neutron radiography very suitable for 2-phase flow imaging in heavy metal casings[4] or water transport in fuel cells [5]. More insight in the physics behind neutron radiography and the experimental setup will be given in chapters 2 and 3.

1.4 Density measurement techniques

Although density is easily defined and widely used as a unit, ways to measure the density of a material, especially of a fluid, are less evident. It is trivial to calculate the average density of something by obtaining the volume and the weight of an object, but to measure the internal density field is very complex in many cases. In the subsections below a few existing measurement techniques are discussed. These techniques are all based on light rays and therefore the medium should be opaque.

1.4.1 Schlieren photography

With Schlieren photography variations in the refractive index caused by density gradients are used to form an image of relative density changes[9]. As shown in figure 4, a knife edge is placed just below the focus point, blocking in uniform density half of the incoming light rays. Light rays that are deflected due to a positive or negative density gradient in the normal direction of the knife edge will be blocked to a respectively higher and lower extent by the knife edge, resulting in darker and lighter patches on the screen. It is not possible to get an accurate absolute density field in this way, but it is a suitable technique to visualise density variations within a sample.

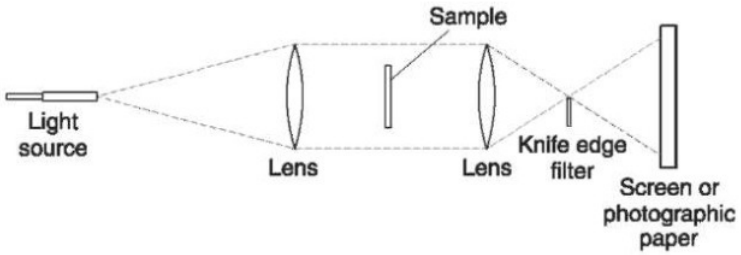

Figure 4: Scheme of the Schlieren photography method.

1.4.2 Moiré deflectometry

In Moiré deflectometry the deformation of a known image gives a measure for the density gradient. This phenomena can be seen in daily life when looking for example at the landscape trough the air behind the exhaust of an airplane or above a burning candle. When the undistorted image is known, for example a grid of black and white squares, the density gradient can be calculated.

1.4.3 Interferometry

In interferometry the phase change of optical waves when they are going through a density field is used to make an image[8]. When the optical beam is aligned with a reference beam an interference pattern occurs where the light that got a phase shift of half a wavelength will die out. Therefore when the test cell is empty the right image will be completely lighted and the top image completely dark, since there will be a phase shift between the 2 bundles in the top image. In figure 5 a setup of Mach Zehnder interferometry is shown.

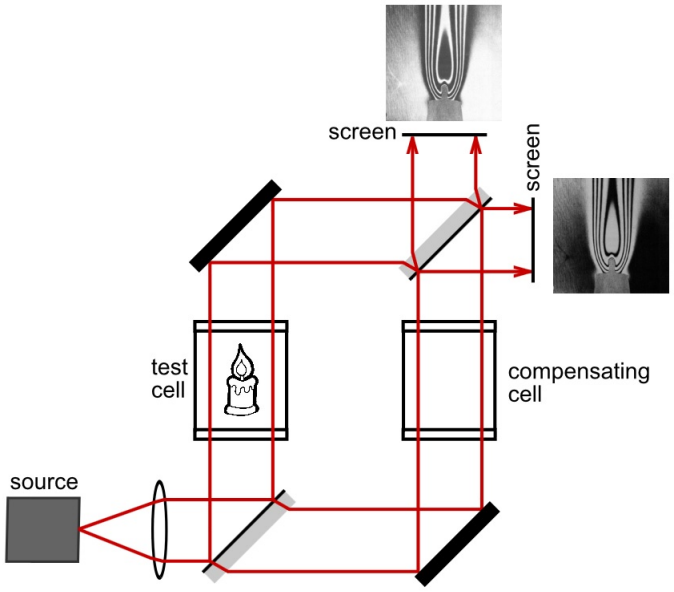

Figure 5: Scheme of Mach Zehnder interferometry.

1.5 Research question

None of the density measuring techniques as described above measure the absolute value of the density, only the relative change in density. Furthermore these techniques all use light, limiting the materials of the container suitable for these techniques to only transparent materials. At the high pressures and temperatures needed to get supercritical water, the constraint of a transparent container is a big downside. Neutron radiography would not have this constraint, as some though materials, like aluminium, are almost completely transparent to neutrons. The following question is therefore investigated in this thesis:
Is it possible to measure the density of supercritical fluids with neutrons? and if so what are the optimal settings to get a clear density field?
To answer this question a computer model was used to acquire the sensor specifications and an experimental setup was build to test the sensor design.

1.6 Thesis outline

In the next chapter a further understanding of the underlying theory of neutron interactions and some calculations on which factors are relevant in the sensor design are outlined.
Chapter 3 provides more details on the computer model used and the experimental setup, next to an outline on the calibration of the experimental setup. In chapter 4 the results are outlined and discussed In chapter 5 recommendations for further research are given. After which in chapter 6 conclusions are drawn. Lastly in Appendix A, a simple example of the method used to remove scatter blurr is given and in Appendix B, a detailed calculation is given on how the normalization factor is fitted.

2 Theory

In this chapter an overview will be given of the theory behind neutron interactions by discussing the microscopic and macroscopic cross sections. This theory will be expanded to formulate usable formulas specifically for the experiments performed for this thesis. A more comprehensive explanation of the theory discussed in this chapter can be found in various literature, a good overview is for example given in Nuclear reactor analysis [1]

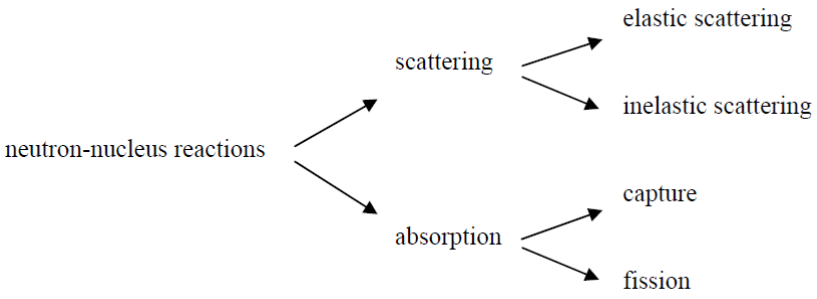

Figure 6: Different types of neutron-nucleus interactions.

2.1 Microscopic cross sections

Because a neutron has no charge, coulomb forces do not play a role, so when calculating the path of an individual neutron the only factor which has to be taken into account is the possibility that the neutron will interact with another atom. The classical way to look at this interaction is to calculate if a neutron goes through the geometrical cross section of an atom, the same way the path of a billiard ball would be calculated. Due to quantum mechanical effects and resonances though, also a neutron passing outside the geometrical cross section of an atom can interact with this atom. To take these effects into account the microscopic cross section σ is introduced:

$$R = \sigma I N \tag{1}$$

with R the interaction rate $[cm^{-2}s^{-1}]$, I the neutron beam intensity $[cm^{-2}s^{-1}]$ and N the number of atoms in a plane $[cm^{-2}]$.
The microscopic cross section typically lies in the order of $10^{-24}cm^2$, which can be expressed as a so-called barn. When a neutron interacts with an atom several things can happen, divided into two main groups: scattering and absorption. In figure 6 the different events are shown. The microscopic cross section strongly depends on the neutron energy and the nucleus type. Furthermore the cross sections associated with specific types of interactions can be added to get the total cross section.

2.2 Macroscopic cross sections

Equation (1) is only valid in a thin layer where no atoms are shielded by others. Deeper in the material the neutron beam will be smaller since some neutrons already reacted with the material and therefore the reaction rate will be lower. To calculate the intensity of the neutron beam in the spatial domain a budget equation can be derived:

$$\sigma_t I N dx = -dI(x) = I(x) - I(x + dx) \tag{2}$$

The spacial gradient is given by:

$$\frac{dI}{dx} = -N\sigma_t I(x) \tag{3}$$

With the boundary condition that $I(0) = I_0$ the following expression for the neutron beam intensity can be derived:

$$I(x) = I_0 e^{-N\sigma_t x} \tag{4}$$

the exponent is often expressed as the macroscopic cross section $\Sigma_t = N\sigma_t$, with dimension $[m^{-1}]$. If equation (4) is divided by I_0 one gets the probability that a neutron travels a distance x through the material without interacting with it:

$$\frac{I(x)}{I_0} = P(x) = e^{-\Sigma x} \tag{5}$$

Equation (5) is key in this thesis, as this equation expresses the relation between neutron intensity and sample thickness. This relation can be rewritten to give a direct relation between intensity and density:

$$\frac{I(x)}{I_0} = e^{-\Sigma x} = e^{-N\sigma x} = e^{-\rho x \sigma / u} \tag{6}$$

with N the amount of atoms in a square centimeter, σ the microscopic cross section, x the thickness of the sample, ρ the density of the material and u the atomic weight.
With equation (5), both the probability that a neutron will travel a distance x without interacting can be calculated, as well as the probability that a neutron will interact within a distance dx:

$$P_2(x) = 1 - \frac{I(x + dx)}{I(x)} = 1 - \frac{I(x) + \frac{dI(x)}{dx}dx}{I(x)} = 1 - 1 - \frac{1}{I(x)}\frac{dI(x)}{dx}dx = \Sigma dx \tag{7}$$

With equations (5) and (7) the mean free path, λ, can be calculated. This is the average length a neutron will travel before interacting.

$$\lambda = \int_0^\infty x P(x) P_2(x) dx = \int_0^\infty x e^{-\Sigma x} \Sigma dx = \frac{1}{\Sigma} \tag{8}$$

Combining equation (8) and (5) shows that the intensity at distance λ in the material has dropped with a factor e.

2.3 Intensity differences

The objective of this thesis is to investigate the feasibility of measuring a density field. In the last section a relation between the density and neutron intensity was shown. A change in density will result in a change in intensity of the measured neutron beam. When the difference in intensity for a given change in density becomes larger, it will be easier to measure that density change. In other words the contrast of the sensor becomes better. This section will look into maximizing the contrast.
When two beams with the same intensity go through the same material at different spots with different densities, the difference in intensity can be calculated in the following way:

$$\Delta I = I_0(e^{-\rho_1 x\sigma/u} - e^{-\rho_2 x\sigma/u}) \tag{9}$$

From equation (9) it can be seen that taking the limit of x to zero or infinity both result in the intensity difference going to zero. This makes sense since a limit to zero means that both beams do not interact with the sample at all and a limit to infinity means that the sample is so thick that every neutron reacts with the sample, despite the value of the density. The intensity difference can be maximized by changing the thickness, x, of the sample:

$$\frac{d\Delta I}{dx} = 0 \Rightarrow x_{max} = \frac{ln(\rho_2/\rho_1)u}{(\rho_2 - \rho_1)\sigma} = \frac{ln((\rho_1 + \Delta\rho)/\rho_1)}{\Delta\rho}\frac{u}{\sigma} \tag{10}$$

Using the result of equation (10) into equation (6) gives the absolute intensity for which there is a maximum difference in intensity.

$$\frac{I_{max}}{I_0} = \frac{I(x_{max})}{I_0} = \left(\frac{\rho + \Delta\rho}{\rho}\right)^{-\rho/\Delta\rho} \tag{11}$$

$$\rho >> \Delta\rho \Rightarrow \frac{I_{max}}{I_0} = \frac{1}{e} \tag{12}$$

Since this is exactly the intensity at the relaxation length we can state that:

$$x_{max} = \lambda = \frac{1}{\Sigma} \tag{13}$$

Using the result of equation (10) into equation (9) gives the maximum amount of intensity difference:

$$\frac{\Delta I_{max}}{I_0} = \frac{\Delta\rho}{\rho + \Delta\rho}\left(\frac{\rho + \Delta\rho}{\rho}\right)^{-\rho/\Delta\rho} \tag{14}$$

Equation (14) does not depend on the cross section of the material but purely on the relative change in density. This implies that changing the material or energy of the neutrons will not change the maximum contrast, however, they will of course change the thickness at which this maximum contrast appears, due to equation (13). Furthermore, it can be seen that the maximum contrast becomes lower when the density increases. To get the best contrast over a specific range of densities the highest density in that range should be taken for ρ in the equations above.

2.4 Uncertainty

In the previous section the conditions for maximum contrast were calculated. This contrast is lowered by uncertainties, caused by fluctuations in the intensity of the incoming neutron beam and the measuring uncertainty of the neutron sensor. In this section the relation between this uncertainty and the measuring time will be investigated.
By studying the temporal fluctuations in the measurements of the incoming bundle, both the uncertainty of the incoming bundle as the uncertainty of the neutron sensor can be measured. In the equation below a normalized standard deviation is defined for measurements for the duration of 1 second:

$$\sigma_1 = \sqrt{\frac{1}{N-1}\sum_{i=1}^{N}\frac{(x_i-\overline{x})^2}{\overline{x}}} \tag{15}$$

where x_i is a specific measurement and $\overline{x}$ the average over N measurements.
Assuming a Gaussian distribution for the overall uncertainty gives an equation for the value of the standard deviation as function of measuring time:

$$\sigma_t = \frac{\sigma_1}{\sqrt{t}} \tag{16}$$

with t the measuring time in seconds.
To be able to differentiate between two different densities, the ratio between the standard deviation and measured intensity difference should not be too high. If the "3-sigma rule" is used, i.e. a 99.7% certainty that the measured density does not differ more than $\Delta\rho$, the following relation applies:

$$3\sigma_t = \frac{\Delta I_{max}}{I_0} \tag{17}$$

By combining equation (14), (16) and (17) the minimum measurement time needed to measure a difference of $\Delta\rho$ with 99.7% certainty is:

$$t = \left(\frac{3\sigma_1\rho}{\Delta\rho}\left(\frac{\rho+\Delta\rho}{\rho}\right)^{\rho/\Delta\rho}\right)^2 \tag{18}$$

Equation (18) can be simplified by using $\Delta\rho = \eta\rho$:

$$t = \left(\frac{3\sigma_1}{\eta}(1+\eta)^{1/\eta}\right)^2 \tag{19}$$

In which η is the relative density difference.

3 Setup

This chapter will first describe the computational model that was used. In the second part, the experimental setup and calibration method are given.

3.1 Serpent

Neutron simulations done in this research have been preformed with Serpent v2.1.12 [13]. Serpent is a three-dimensional neutron Monte Carlo code using continuous energies. To simulate the neutron bundle, the source in Serpent was defined by 17 different energies bins, following the Maxwell-Boltzmann distribution for thermal neutrons. These bins are shown in table 1.

energy bin $[10^{-2}eV]$	ratio [%]
0.0-0.5	0.5703
0.5-1.0	3.7459
1.0-1.5	8.7215
1.5-2.0	13.4212
2.0-2.5	16.1342
2.5-3.0	16.2027
3.0-3.5	14.0559
3.5-4.0	10.7368
4.0-4.5	7.3084
4.5-5.0	4.4685
5.0-5.5	2.4678
5.5-6.0	1.2361
6.0-6.5	0.5632
6.5-7.0	0.2340
7.0-7.5	0.0888
7.5-8.0	0.0308
8.0-2Mev	0.0137

Table 1: Energy bin distribution used in Serpent.

In the simulated bundle, neutrons have a velocity, according to their assigned energy, solely in the x-direction. This means that the simulated bundle is perfectly parallel. They were all created in a source plane, 5x5cm wide in the y/z-direction. Behind the source plane a numerical sample is placed, also with a size of 5x5cm. To simulate the sensor output of the experimental setup the reaction rate in a thin plate of Lithium is recorded. In figure 7 a drawing of the setup in Serpent is shown. The JEFF-3.1.1 [10] database is used as a cross section library. This database stores the cross sections and scatter angle distributions for different neutron interactions.

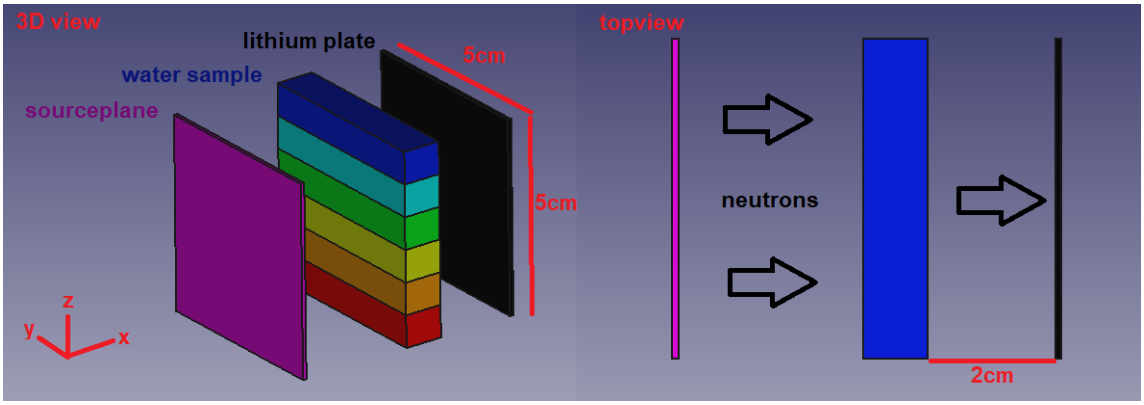

Figure 7: Setup in Serpent.

3.2 Experimental setup

To verify the theoretical and computational results of this research an experimental test setup was build. In the chapters below the test setup will be explained. A detailed explanation is given about the neutron sensor and the method of calibrating and processing the data from the sensor.

3.2.1 Scatter material

In the experimental setup a thermal neutron beam [12] from the HOR reactor in Delft is used as a neutron source. This neutron bundle has a Maxwell-Boltzmann distribution, which is described by:

$$f(\epsilon) = \sqrt{\left(\frac{m}{2\pi kT}\right)^3} 4\pi\epsilon^2 e^{-\frac{m\epsilon^2}{2kT}} \tag{20}$$

Where ϵ is the neutron energy.
In this distribution the most probable neutron speed is given by:

$$V_p = \sqrt{\frac{2kT}{m}} \tag{21}$$

Which is roughly 2.2km/s or 0.025 eV.
The overall cross section for this energy distribution can be found by integration:

$$\sigma_{mb} = \int_0^\infty f(\epsilon)\sigma(\epsilon)d\epsilon \tag{22}$$

The JEFF 3.2 cross section library is used to find the energy dependence of different cross sections. The overall microscopic cross sections can be found in table 2.

atom	cross section [barn]
^1H	31.27
^{12}C	4.97
^{16}O	3.99

Table 2: Overall microscopic cross sections,σ_{mb}, for a Maxwell-Boltzmann neutron energy distribution.

As can be seen in table 2, hydrogen has a significantly higher microscopic cross section compared to oxygen or carbon. Therefore it can be expected that the hydrogen atoms in water account for the biggest contribution to neutron interaction. To mimic the scattering effect of water, plates of polyethylene were used as a sample material. Because polyethylene is solid at room temperature it is much easier to vary the thickness of the material. Polyethylene is a plastic with solely carbon and hydrogen atoms and just like water has a high fraction of hydrogen atoms. Plates of 2mm were used and when a

different thickness was needed the plate was milled to the desired thickness. In figure 8 a picture of the eperimental setup is shown. In some experiments not the whole neutron bundle, but only a very small bundle was required. In this case a plate made out of a strong neutron absorber with a pinhole, 750 μm in diameter, was attached to the pipe with the incoming neutron bundle. In the picture it is referred to as pinhole plate.

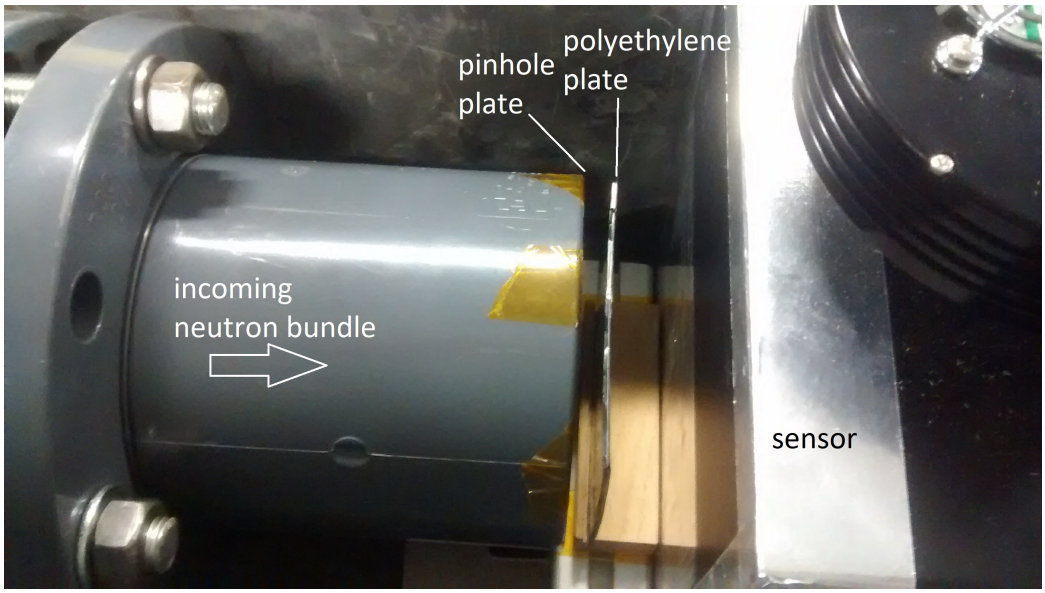

Figure 8: Experimental setup.

3.2.2 Sensor

To measure the incoming neutrons a detector from Neutron Optics [11] is being used. This detector uses lithium to capture neutrons, this reaction has helium and hydrogen as fission products

$$^6Li +^1 n \rightarrow^3 H +^4 He + 4.79MeV \tag{23}$$

The fission products are thereafter absorbed by a scintillator (ZnS), as a result of this absorption the scintillator emmits photons which can be detected by a CCD. To protect the CCD, the CCD is not placed behind the scintillator in the neutron beam, but a mirror reflects the emmitted fotons to the CCD outside of the neutron beam.
The lithium and zinksulfide are mixed in a thin sheet called the scintillator screen. The thickness of the the scintillator screen determines the effectiveness of the detector, since a thicker screen has a higher chance of capturing a neutron, and therefore detecting it. On the other hand a thicker screen also reduces the resolution of the image [7]. The detector used in this experiment has a 200 μm scintilator screen and a pixel size on the CCD of 110 μm.

3.2.3 Calibration

Measuring neutron intensity with a scintilator screen and CCD introduces errors, which will be addressed in this section. First for some pixels the outcome does not seem to give any plausible results. When measuring without an incoming neutron bundle these pixels light up. Since the location of these pixels is the same for different measurements, the cause of this error must be in the measuring device. Most of these errors occur due to the fact that these pixels are broken on the CCD [11]. From now on these pixels will be referred to as *non-working pixels*. A measurement were there is no incoming neutron bundle will from now on be called a *dark measurement*. Figure 9 shows a histogram with the occurrences of photon intensity on the y-axis for a dark measurement. As shown there is no clear distinction between working and non-working pixels. The vast majority of the pixels, more then 98%, has an intensity of less then 350. All pixels with a higher intensity then 350 at a dark measurement are defined as non-working.

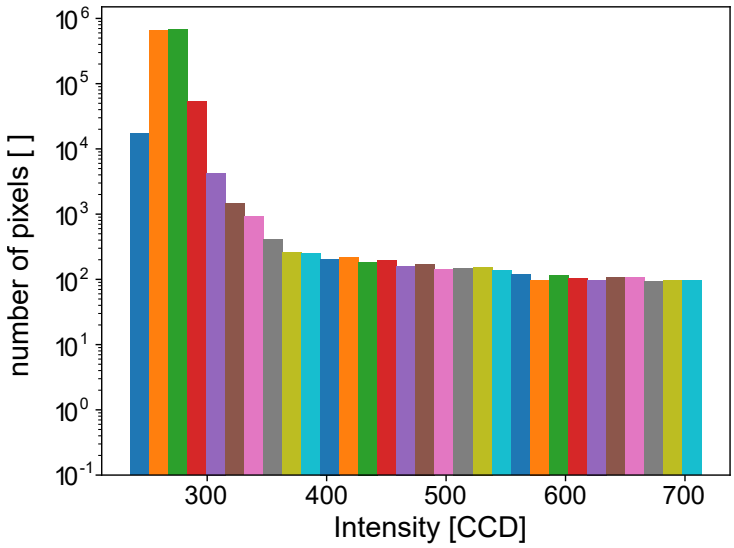

Figure 9: Histogram of the CCD output of the sensor for a dark measurement.

Besides non-working pixels, the working pixels also have an offset error. In Figure 10 the cumulative output of the CCD when the detector is irradiated by the neutron bundle is plotted for different measuring times. As shown, a linear plot through these points does not go through the (0,0) point. The fitted offset does exactly match the cumulative CCD output for a dark measurement. The offset is not increasing in time, so each dark measurement, independent of measuring time, gives the same result. Therefore, as with the non-working pixels, this offset must also have an internal cause.

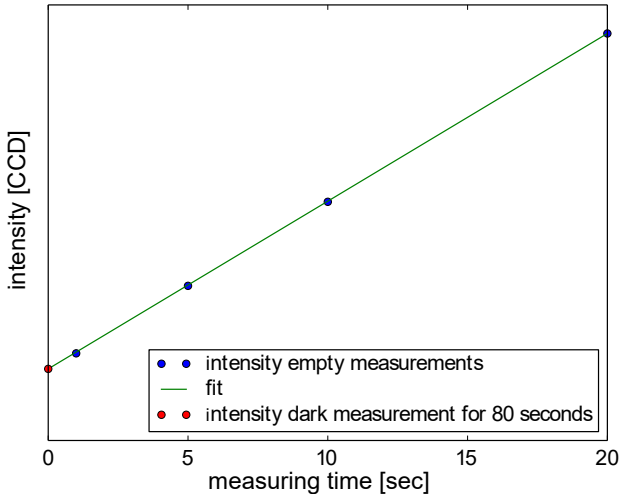

Figure 10: Cumulative CCD output of an empty measurement for different measuring times.

Because of the non-working pixels and offset error the sensor needs to be calibrated. A flowchart of the used calibration procedure is given in figure 11. As shown two calibration measurements are needed: A dark measurement, where the sensor output is measured without an incoming bundle, and an empty measurement, where the sensor output of the neutron bundle without any sample is measured. From the dark measurement the non working pixels and offset error are acquired. With these errors known, the intensity of the incoming bundle can then be calculated from the empty measurement.

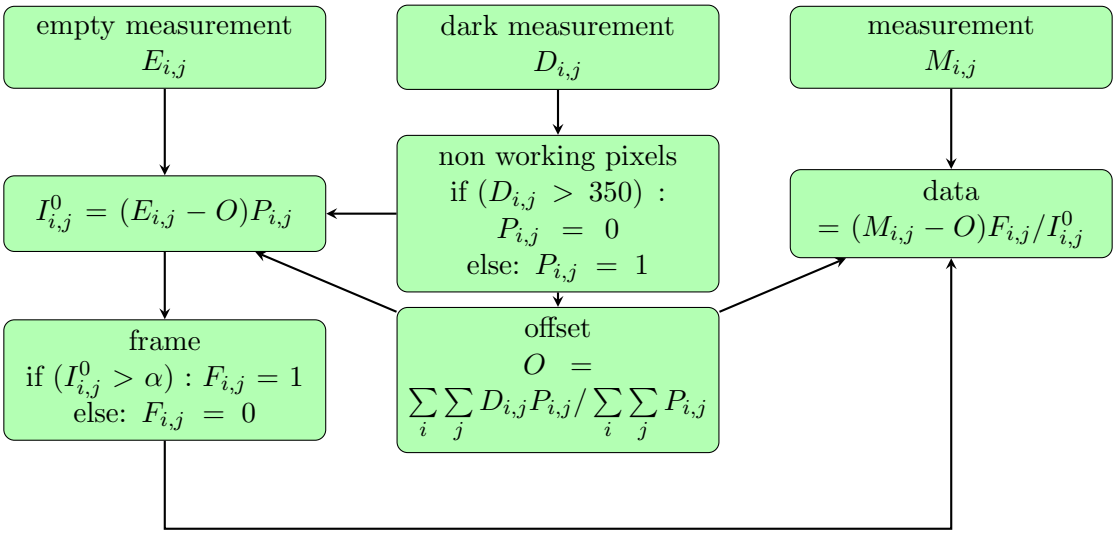

Figure 11: Flow chart of compensation for non working pixels and the offset error of the measuring device. α is a threshold for defining the measurement frame.

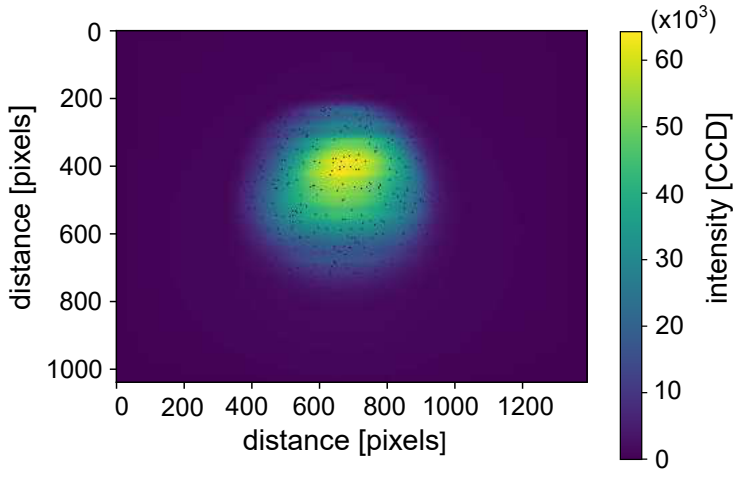

Figure 12: CCD output of an empty measurement, meaning the sensor was put in front of the bundle without any sample. The figure shows the average value of 60 20second measurements, after compensating for the offset.

The CCD output is stored by the sensor in 16bits integers. To avoid data overflow, the maximum exposure duration is set to 20 seconds. In figure 12, the time averaged spacial intensity of the empty measurement is shown, this is the average CCD output for 60 measurements of 20 seconds duration after compensation for errors as described in figure 11. As shown the intensity of the bundle is not uniform in the spacial domain, but varies significantly. Since there is no clear edge of the bundle, defining a clear spacial window were the neutron bundle is present is challenging. However this window, from now on called the measuring frame, is needed to define which pixels to include in the measurement. To help defining the measuring frame, the relative standard deviation $\sigma^r_{i,j}$ is introduced:

$$\sigma^r_{i,j} = \frac{\sigma_{i,j}}{I_{i,j}} \tag{24}$$

Where $\sigma_{i,j}$ is the standard deviation over the different measurements for a specific pixel and $I_{i,j}$ the average intensity of that pixel.
The relative standard deviation is a direct measure for the uncertainty component of the neutron bundle when comparing two measurements. To limit this uncertainty the measuring frame should only include measurements where the relative standard deviation of the incoming bundle is below a certain threshold. Defining the measuring frame directly from the relative standard deviation would result in an noncontinuous frame without a clear edge, this is undesirable because with a clear measuring frame measurements on different locations can be added together to cover a larger area. In contrast to the

relative standard deviation the intensity of the bundle does gradually decline from the center of the bundle outwards, therefore it is easier to define the measuring frame by the intensity of the bundle. In figure 13 for each pixel the relation between the average intensity and the relative standard deviation is plotted. As shown the higher the intensity the lower the relative standard deviation, so using the intensity of the bundle would still result in a measuring frame with a low relative standard deviation. The higher the threshold the lower the average relative standard deviation, but setting the threshold too high would result in a too small frame. From this picture a CCD value of 18000 seems like a good threshold for this measurement.

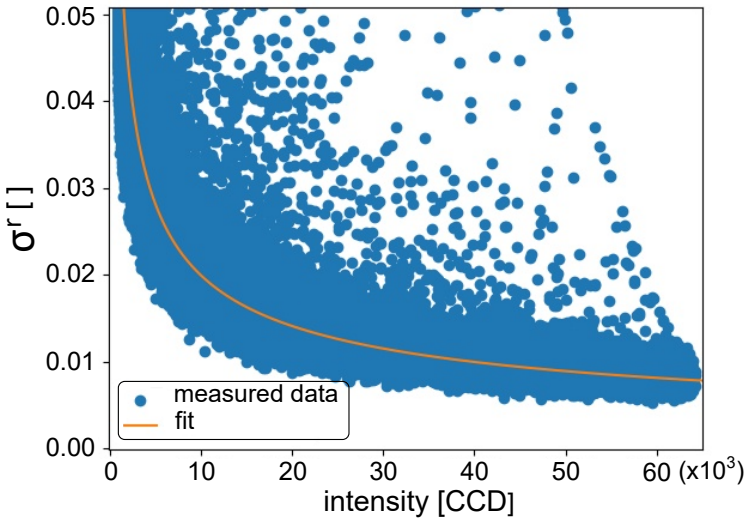

Figure 13: Relation between measured intensity and relative standard deviation, every blue dot is representing a pixel on the sensor. The yellow line is a fit.

4 Results and discussion

In this chapter the results of the experiments are presented and discussed. The aim of the experiments is to accurately measure the thickness of a slab of material. An experiment is conducted where a polyethylene plate is put in front of a neutron bundle with the neutron sensor far away from the sensor. Secondly a situation is modelled computationally where the sensor is put close behind the slab. Lastly the computational model setup, with the sensor close behind the slab, is validated experimentally, again with a polyethylene sample.

4.1 Experimental setup, dealing with divergence

The objective of this thesis is to investigate the feasibility of measuring density differences in supercritical water. As supercritical water has a very high temperature and pressure, polyethylene was chosen as a test substrate as it can be used at room temperature and normal atmospheric pressure, and most importantly, its molecular structure has a high ratio of hydrogen atoms similar to water.
Making high density variations in polyethylene is not possible, but as was shown in section 2.2, varying the thickness of the plate has the same effect on neutron interaction as varying the density. The mean free path of thermal neutrons in polyethylene is around 2mm, so a plate of this thickness is used. To mimic density differences, six 3mm wide layers with uniform thickness were milled in the plate with from top to bottom a thickness of 1.9 mm, 1.8 mm, 1.7 mm, 1.5 mm, 1.0 mm and 0.5 mm.
In this first experiment, the sensor was placed approximately 20 cm behind the plate to minimize the effect of scattering. Results of this measurement are shown in figure 14. In figure A the intensity of the incoming bundle is shown with no plate in place in front of the sensor. In figure B the intensity is shown with the plate in place. Figure C shows the ratio between A and B, given by B/A. A measuring window is introduced in figures C&D, as explained in section 3.2.3. Lastly, figure D shows the calculated thickness of the plate using equation (6). Figure D clearly shows the 6 layers and the measured thickness corresponds well to the actual thickness. On the edges though, some blur can be seen, most clearly visible on the bottom layer of figure D. This blur is caused by the divergence of the bundle. The incoming neutron bundle is not completely parallel but diverges slightly, which causes neutrons that cross the polyethylene plate at the same position to end up on slightly different spots on the sensor. This effect will be smaller if the sensor is placed closer to the plate. This will be shown in the second set of experiments.

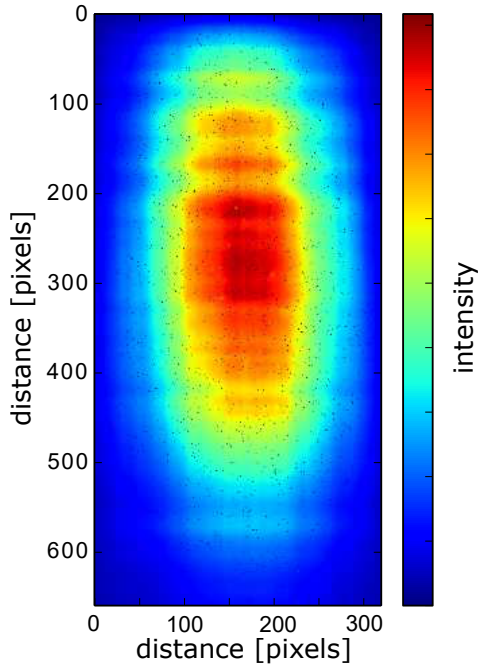

Figure A: intensity incoming bundle

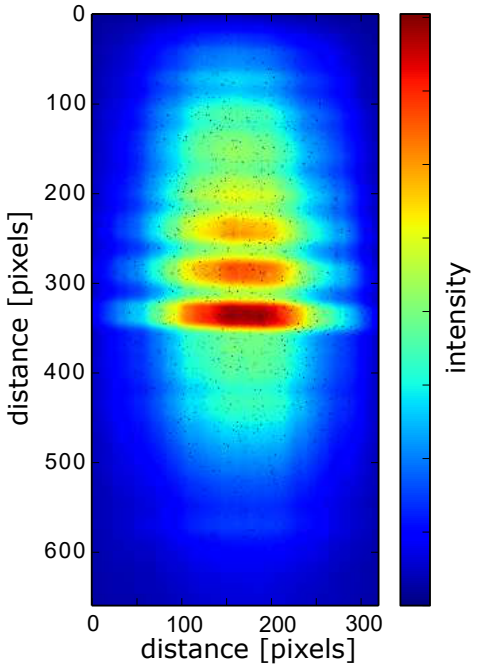

Figure B: intensity with plate

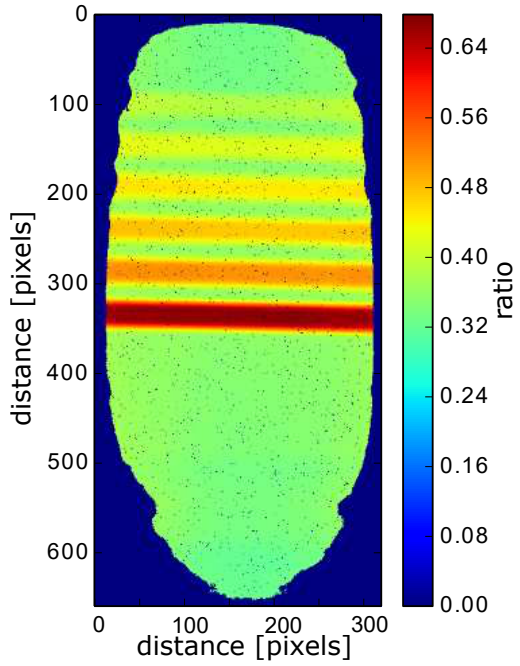

Figure C: ratio between A and B

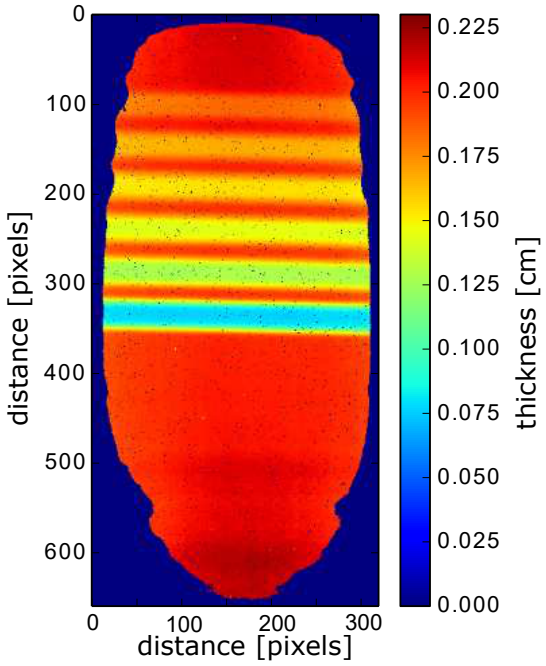

Figure D: calculated thickness [cm]

Figure 14: radiography of a polyethylene plate of 2mm with horizontal cavities of different thickness, from top to bottom: 1.9mm, 1.8mm, 1.7mm, 1.5mm, 1.0mm, 0.5mm. Figure A shows the incoming neutron bundle (empty measurement), figure B shows the neutron intensity with the sample, figure C shows the ratio of A and B, B/A and lastly figure D shows the calculated thickness using figure C and equation (6).

4.2 Computational setup, dealing with scattering

As shown in the previous section the sensor has to be as close as possible to the sample, because the slightly divergent bundle causes blurring. The objective of this research is to measure fluids in the supercritical state, a casing around the sample is required, because of the high pressure involved in these fluids. This casing makes it impossible to measure directly behind the sample. In this paragraph therefore a distance between the sample and the sensor of 2 cm is taken, as 2 cm is a feasible thickness for such a casing.
Putting the sensor this close to the sample however gives another type of blurring: blurring due to scattering. Neutrons scattering with a small angle will still hit the sensor and therefore invoke an uncertainty in the measurement. A simulation of the sensor output in Serpent has been performed for a neutron bundle going through a slab of supercritical water with vertically six different layers of uniform densities, varying from 0.5 kg/dm^3 to 0.3 kg/dm^3. As shown in figure 15 the simulated sensor output is not constant over the layers of uniform density. For example the neutron intensity within the top layer varies more than 12 percent. The neutron intensity stands for the amount of neutrons hitting the sensor per second at a given pixel. Since the neutron intensity is not directly related to the density, due to scattering, as figure 15 shows, the density field can not immediately be calculated from this result.

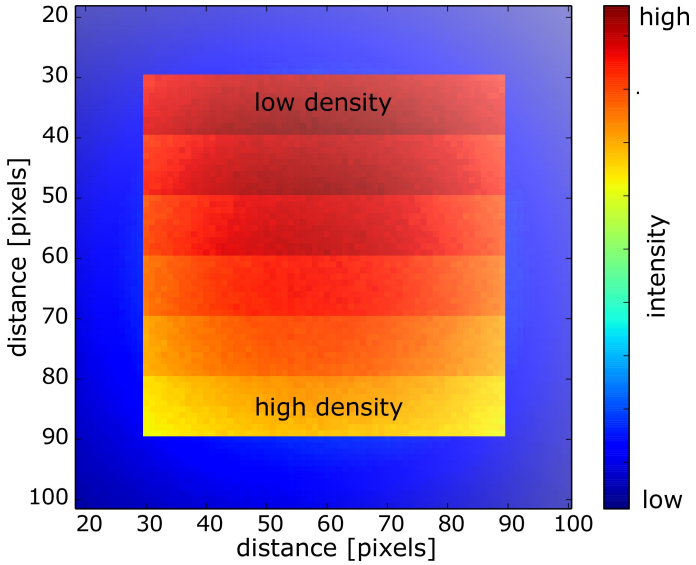

Figure 15: Neutron intensity on a plane 2 cm behind a slab of water with vertically six different layers of uniform density from 0.5 kg/dm^3 to 0.3 kg/dm^3 (simulated with Serpent).

The result of an incoming neutron bundle can also be seen as a superposition of the result of multiple thin bundles, since neutrons do not have any interaction with each other. To further study the non-uniformity results of the last section, the interaction of

a set of multiple thin bundles will be explored. For this, a simulation is performed where a neutron bundle, with a very small diameter, is send through a slab of water of uniform density. Without putting the slab in front of the sensor the bundle would just hit 1 pixel on the sensor. With the slab in place, scattering will occur. In the left hand graph of figure 16 the normalized intensity is plotted against the radial distance over which the neutrons scatter. The data is normalized according to equation (25), such that the sum of the intensity over a given data set is 1.

$$\alpha \sum_{i,j \neq 0,0} I_{i,j} = 1 \tag{25}$$

These normalized intensities, shown in figure 16, show that the shape of the data sets does not depend on the density of the material. Since the thickness of the slab is around the mean free path, the amount of neutrons that scatter multiple times is too small to affect the shape of the radial intensity. The graph on the right shows the average intensity as a function of scatter angle instead of distance. To get the distribution of intensity for scatter angles, the average has to be compensated for the fact that larger angles scatter over a larger area:

$$f_{angle} = \frac{I_{angle} 2\pi r}{\int I_{angle} 2\pi r dr} \tag{26}$$

where r is the radial distance.
In the right hand graph of figure 16 this is represented by the green line. The most likely scatter angles are roughly between 10 and 30 degrees. These results follow from the data in the JEFF311 [10] database that Serpent uses.

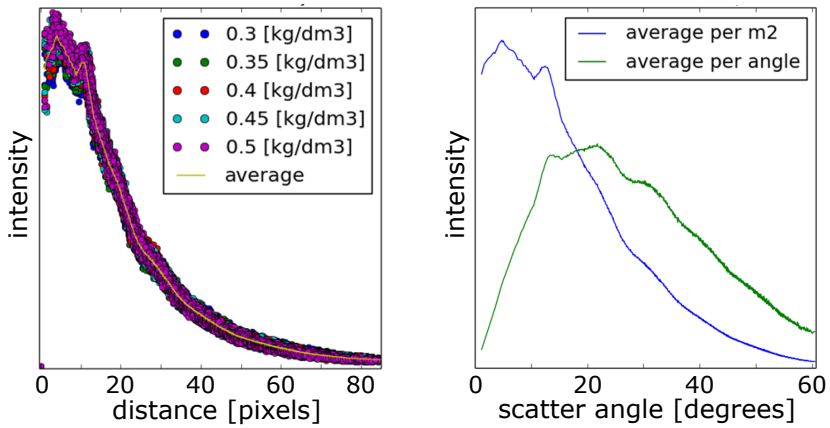

Figure 16: Normalized radial intensity for a pixel wide incoming neutron bundle (simulated with Serpent). The yellow line in the left figure is the average result over all data sets. All data is normalized such that the integral is 1.

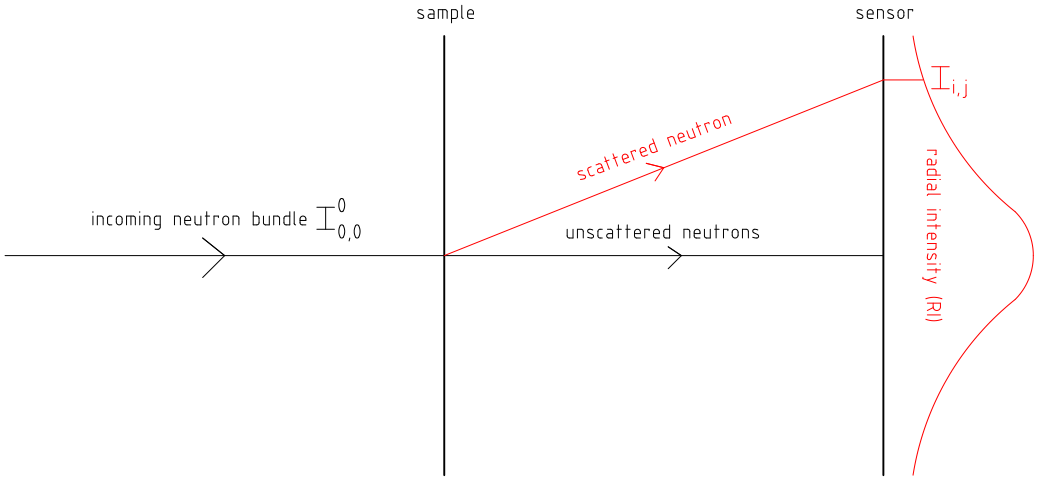

Figure 17: Schematic drawing of the radial intensity, in the drawing $I^0_{0,0}$ is a delta function that without a sample would only hit the sensor at pixel 0,0

The average in the left hand graph of figure 16 is the normalized radial distribution of neutron intensity for a single beam. This normalized radial intensity solely depends on the radial distance and will be called the radial distribution, RD(r). In figure 17 a schematic drawing is given of the radial intensity, the distribution of scattered neutrons for a single neutron beam. The shape of the radial intensity is defined by the radial distribution, but the actual neutron intensity at a given radial distance for a single beam also depends on the intensity of the incoming bundle, I^0, and the density, since a higher density will result in more scattered neutrons. This dependence on the density will be represented by the normalization factor, NF:

$$I_{i,j} = I^0_{0,0} * NF(D_{0,0}) * RD(\sqrt{i^2 + j^2}) \tag{27}$$

with $I^0_{0,0}$ a delta function representing the incoming neutron bundle, $NF(D_{0,0})$ the normalization factor, the factor of neutrons that scatter and still hit the sensor, $D_{0,0}$ the density of the sample at 0,0 and RD the radial distribution function.
The normalization factor is not a simple linear function: in the extreme cases of a density of 0 or an infinitely high density the contribution will in both cases be zero. The normalization factor will be defined by the following function:

$$NF(D_{0,0}) = \frac{\sum_{i,j \neq 0,0} I_{i,j}}{I^0_{0,0}} \tag{28}$$

with $I^0_{0,0}$ a delta function only hitting the sensor at i,j = 0,0 and $I_{i,j}$ the radial intensity for the density at 0,0.
The normalization factor can be seen here as the fraction of the incoming intensity that scatters and still hits the sensor. The contribution to the intensity of a specific pixel

at position i,j, by incoming neutrons aiming at position k,l can be expressed by the following equation:

$$I_{i,j} = I^0_{k,l} * NF(D_{k,l}) * RD\left(\sqrt{(k-i)^2 + (l-j)^2}\right) \tag{29}$$

Where the indexes i,j and k,l refer to a specific pixel location, I^0 is the incoming intensity, NF the normalization factor and RD the radial distribution
In figure 18 the normalization factors for the different densities are plotted. In this graph the total intensity of the scattered neutrons increases with increasing density. This makes sense since a higher density means more neutrons collide and scatter. If much higher densities or ticker samples would have been used the intensity would become lower for increasing density, because now the probability that neutrons scatter multiple times to larger angles or get absorbed is increasing faster than the probability that neutrons scatter towards the sensor. For the thickness considered in this work, as calculated in equation (10), however, an increasing normalization factor for increasing density is a typical result. A curve can be fitted through the points to get an expression for the normalization factor as function of the density. In Appendix B an analytical approach is introduced to derive an expression for this fit.

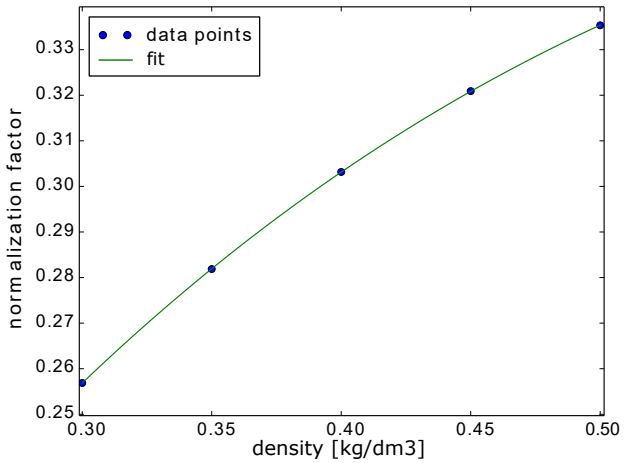

Figure 18: Normalization factor for the incoming scattered neutron intensity as a function of the density (between 0.3 kg/dm^3 and 0.5 kg/dm^3). Data obtained with Serpent.

Once the shape of the radial intensity distribution (figure 16) is known and the constants for the fit in figure 18 are calculated, a method can be introduced to subtract the scattering blur from the calculated image as presented in figure 15. With a function for the radial intensity, RD(d), the normalization factor, NF($D_{i,j}$), and the initial intensity of the bundle, $I^0_{i,j}$, the intensity on the sensor, $S_{i,j}$, can be calculated when the density, $D_{i,j}$, is given:

$$S_{i,j} = I^0_{i,j} e^{-\Sigma_t D_{i,j}} + \sum_{k,l} I^0_{k,l} * NF(D_{k,l}) * RD\left(\sqrt{(k-i)^2 + (l-j)^2}\right) \tag{30}$$

The first term in this equation (30) represents the neutrons that did not interact with sample. With increasing density the amount of neutrons that do not interact decreases exponentially. The second term is the sum over all scatter contributions from surrounding pixels. To conclude, provided that the radial intensity and the normalization factor are known, the intensity on the sensor can be calculated for a given density field. It is not possible however to reverse the formula to get an explicit expression for the density field. To calculate the density on a specific point the density on all other points must be known first. The density field can be approximated by iteration. Since changing the density in the first term in equation (30) has a much larger effect on the intensity on the sensor than changing the density in the second term, the iteration converges rapidly when for the update of the density field only the first term of equation (30) is taken into account:

$$\begin{aligned} \frac{dS}{dD} &\approx \frac{d}{dD}(I^0 e^{-\Sigma_t D}) = -I^0 \Sigma_t e^{-\Sigma_t D} \\ D_{i,j}^{new} = D^{old} + \Delta S / \frac{dS}{dD} &= D_{i,j}^{old} + (S_{i,j} - M_{i,j}) / I_{i,j}^0 \Sigma_t e^{-\Sigma_t D_{i,j}^{old}} \end{aligned} \tag{31}$$

where M is the intensity of the measured data.
The iteration process is shown in a flow chart in figure 19. In Appendix A a simplified example for the method described above is elaborated.

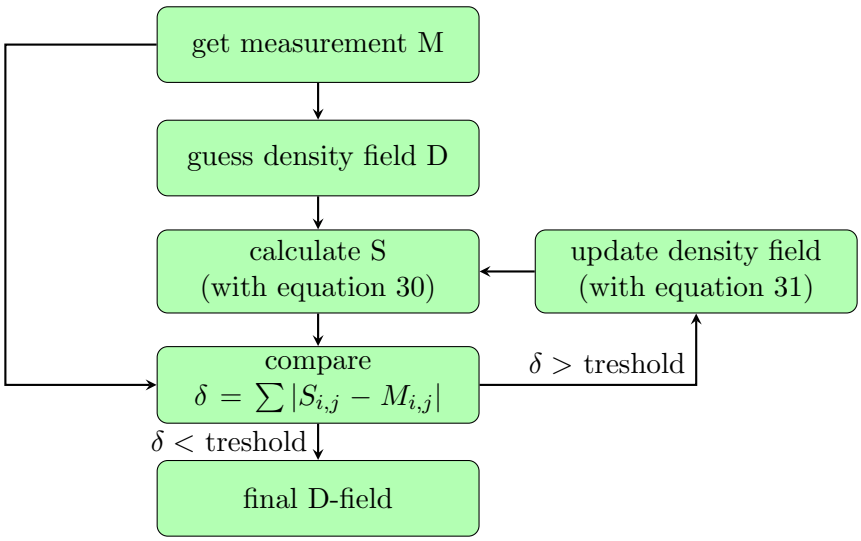

Figure 19: Flow chart of the iteration process.

In figure 20, the reconstructed density field $D_{i,j}$, is shown. One can clearly see the six layers of uniform density. The noise shown in the picture is due to the uncertainty of the neutron bundle in Serpent, which is also clearly visible in figure 15. When the average densities over the layers are evaluated, these values are very close to the real densities,

with errors below 1 percent. This method for removing the scatter blur thus works really well, at least for the output of this simulation.

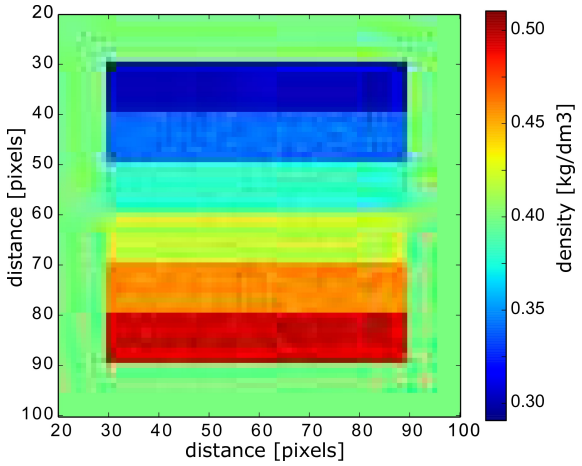

Figure 20: Final density field, calculated with data from a simulation with Serpent, after applying the methodology as described in figure 19.

4.3 Experimental setup, dealing with scattering

In this experiment the procedure explained in the previous section was put into practice. The first step is to measure the amount of blur due to the divergence. For this the bundle is reduced to a small bundle with a strong neutron absorbing material with a small pinhole of 0.75mm in diameter. In figure 22 the radial intensity profile for different distances between the sensor and the pinhole is plotted. The larger distance was not measured but is between 20 and 25cm. Figure 22 shows that the blur due to divergence can be neglected for small distances up to 3.5cm. Further measurements in this section are all done with a distance of 3.5cm between the sensor and the pinhole. Since for small distances the divergence can be neglected, the expected outcome for radial intensity would be a step function, because the strong neutron absorber will block all neutrons that do not pass the pinhole. In the figure this expected outcome is indicated by a dotted line. The reason for the difference between the measured result and the expected outcome must be sought in the sensor, since any effect before the sensor would have resulted in a deviation between the measurement at the pinhole and 3.5cm away from it.

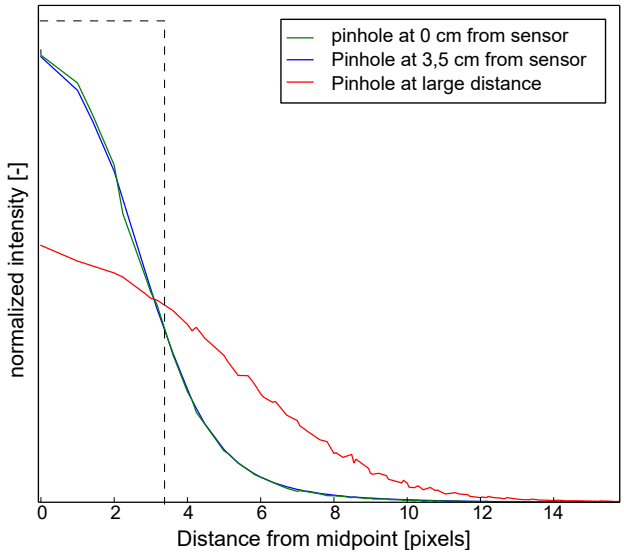

Figure 21: Bundle intensity as a function of the radial distance from the center of the bundle for different distances between the pinhole and the sensor.

A possible explanation for the difference between the expected and measured result in figure 22 can be that the location of the neutron is different from it‘s measured position. As discussed in section 3.2.2, the sensor absorbs neutrons and then sends out an alpha particle. This alpha particle emits light due to the scintilator which is then captured by a CCD. In this process the measured position of the neutron could deviate from the actual position. In the following section this effect will be looked into.

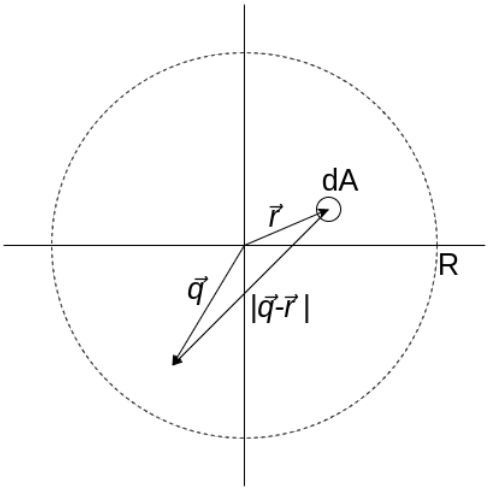

Figure 22: Schematic drawing of the vectors used in equation 33 and 34

4.3.1 Sensor blur

In the previous section a difference was shown between the expected outcome of a pinhole measurement and the actual measurement result. A possible explanation for this can be sought in a deviation between the actual position of a neutron and it's measured position by the sensor. This section will investigate this hypothesis by trying to find a probability function for this deviation and compare this probability function with the measured data.
If assumed that there is a function f that gives the radial probability of a neutron hitting the sensor at r = 0 being detected at position r, with:

$$\int_0^{2\pi} \int_0^{\infty} f(r) r d\theta dr = 1 \tag{32}$$

Furthermore, if assumed that the neutron intensity does not deviate significantly over the pinhole, setting the incoming neutron bundle within a radius R equal to I_{B0}, a small area within the radius R then contributes to the measured intensity at position q with:

$$I_{B0} f(|\vec{q} - \vec{r}|) dA \tag{33}$$

integrating over the whole area with radius R then gives the measured intensity at position q:

$$\int_0^{2\pi} \int_0^{R} I_{B0} f(|\vec{q} - \vec{r}|) r d\theta dr = I_{PQ} \tag{34}$$

this integral cannot be solved since $\vec{r}$ and $\vec{q}$ depend on both r and θ. But in the special case where $q = 0$, at the center of the incoming bundle, the θ dependency disappears and the following integral can be made:

$$\int_0^{2\pi}\int_0^{R} I_{B0} f(|-\vec{r}|) r d\theta dr = \int_0^{2\pi}\int_0^{R} I_{B0} f(r) r d\theta dr = I_{P0} \tag{35}$$

With I_{P0} the intensity at r = 0 with the pinhole, I_{B0} the intensity at r = 0 without the pinhole and R the radius of the pinhole

Using equation (32) and (35), two unknowns in a guess for the function f(r) can be calculated. The following two functions where evaluated:

$$f(r) = Ae^{-Br} \quad \text{an e-power function} \tag{36}$$
$$f(r) = Ae^{-Br^2} \quad \text{a Gauss function} \tag{37}$$

Solving equations (36) and (37) with the integrals (32) and (35) gives a solution for A and B respectively:

$$A = \frac{B^2}{2\pi} \quad \frac{I_{P0}}{I_{B0}} = 1 - e^{-BR}(BR+1) \tag{38}$$
$$A = \frac{B}{\pi} \quad B = -ln(1 - \frac{I_{P0}}{I_{B0}})/R^2 \tag{39}$$

Using these assumptions for f(r) the expected measurement result can be calculated for an incoming radial distribution of a step-function. In figure 23 the calculated radial distribution is plotted for the two assumed functions for f(r), and compared with the measured data. As shown the outcome of these calculations match quite well with the measured data.

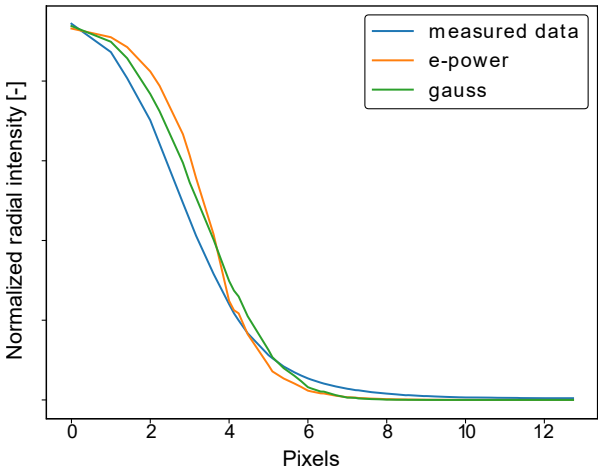

Figure 23: Bundle intensity as a function of the radial distance from the center of the bundle, as well as 2 calculated results for an incoming step-function with different distributions.

4.3.2 Removing sensor blur

As shown in figure 23 the Gauss distribution gives a slightly better result. This function will be used in this section to remove the sensor blur from measurements made with a pinhole and a plate of polyethylene in front of the neutron bundle. The assumption is that after removing the sensor blur the only two contributions will be a uniform circular bundle the size of the pinhole, caused by the neutrons that did not scatter, and the scatter contribution. The goal is to extract the scatter contributions from these measurements and calculate the radial intensity the same way as in the computational case (figure 16).
In figure 24a the radial distributions with a pinhole in place is plotted for different thicknesses of polyethylene. Using the Gauss distribution of equation (37) and the iterative procedure shown in figure 19 an iterative result for the incoming neutron bundle is achieved. In this iterative calculation an initial incoming neutron field is guessed, then the Gauss function is used to calculate the blur caused by the sensor and the resulting neutron field is compared with the actual measurement to update the guess for the incoming bundle.

$$S_{i,j} \stackrel{?}{=} \sum_{k,l} G_{k,l} * f\left(\sqrt{(k-i)^2 + (l-j)^2}\right) \tag{40}$$

with S the data measured by the sensor, G the guess for the incoming neutron field and f the Gauss function derived in the previous section.
Figure 24a represents the data given by the sensor (S in equation (40)) and figure 24b the calculated incoming neutron bundle assuming a Gaussian blur by the sensor (G in equation (40)). As can be seen the result of Figure 24b is much closer to the expected step-function. Still the procedure does not give a close enough result compared with the expected step function. Next to the spikes in the high part of the functions in figure 24b, at a radial distance higher than 4 pixels the graph still shows the highest neutron intensity for the data without a plate of polyethylene. This is not an expected result, as a lower density should result in less scattering and therefore in a lower intensity outside the radial window of the pinhole.
Clearly the sensor blur is reduced in figure 24b, but not completely removed. From this result it is not possible to extract the scatter contribution and find a function for the radial intensity.

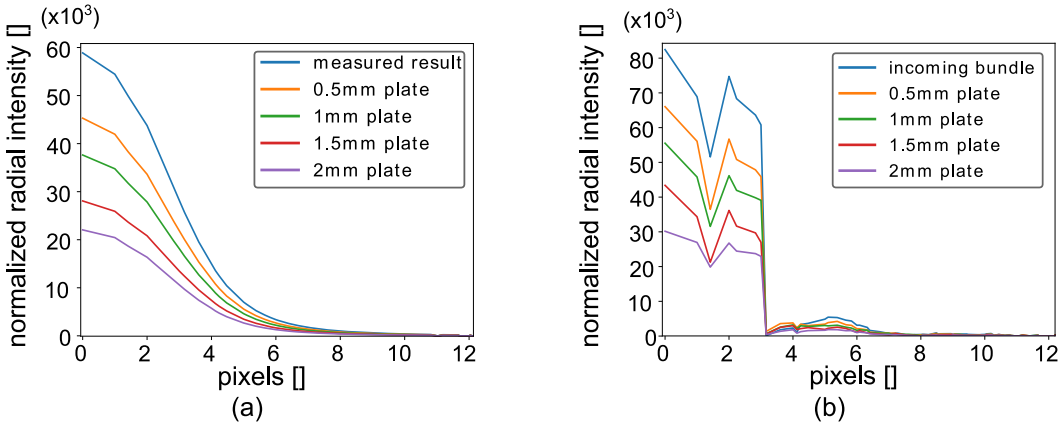

Figure 24: Radial distribution of pinhole measurements with different thickness of polyethylene (0.5mm,1mm,1.5mm,2mm). Measured (a) and calculated with a Gaussian distribution (b).

Since from the result of figure 24 no information can be extracted about the scatter angles of scattered neutrons, the pinhole measurements as described in this section do not help in finding a function for the radial intensity of scattered neutrons. This radial intensity is needed in order to subtract the scatter contribution from the measurements. One alternative strategy is to assume a scatter profile. The most easy to calculate assumption then is a uniform scatter profile. Another option is to calculate a radial distribution using a computational model, for example with Serpent, like was done in section 4.2 and shown in figure 16. It is not possible to use the result of figure 16 as a radial distribution for the experimental case, since an other material was simulated, with another thickness and another distance to the sensor. Making another calculation with Serpent is outside of the scope of this thesis, the next section will therefore show the calculation of the radial distribution on the sensor for a uniform scatter profile.

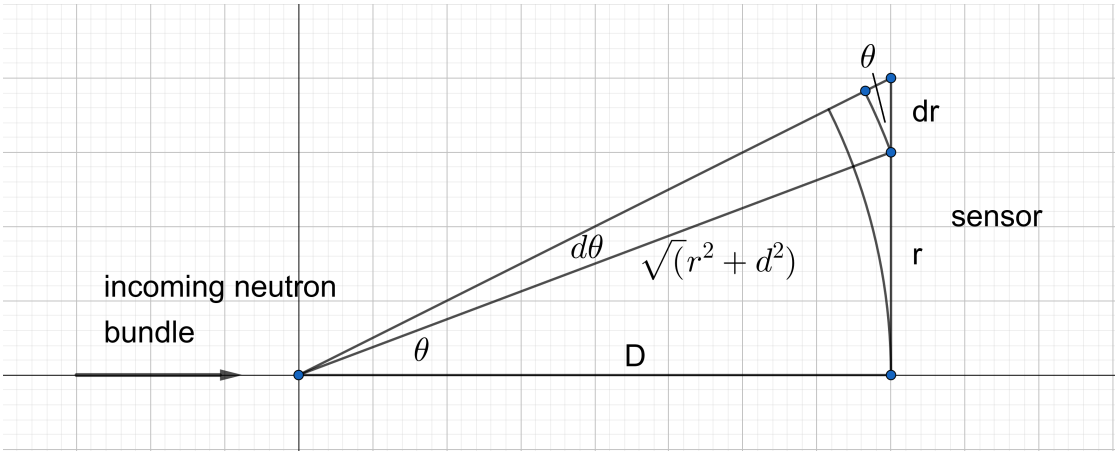

Figure 25: Schematic drawing of an incoming neutron bundle and the scatter angle θ.

4.3.3 Radial distribution for uniform scattering

Since the pinhole measurements did not give a clear result for the radial distribution of scattering, this section will calculate the radial distribution assuming a uniform scatter distribution, this means it is assumed all scatter angles are equally likely.
Looking at figure 25 one could imagine a three dimensional cone with angle θ that is a part of a sphere, where the whole sphere represents all the possible scatter angles. The volume of the cone divided by the volume of the sphere would, in the case of uniform scattering, be the fraction of scattered neutrons that hit the sensor within a radius r.

$$F(\theta) = \frac{V_{cone}}{V_{sphere}} = \frac{1}{\frac{3}{4}\pi r^3} \int_0^{2\pi} \int_0^r \int_0^\theta r^2 sin\theta d\theta dr d\phi = \frac{1}{2} - \frac{1}{2} cos\theta \tag{41}$$

When the cone is increased with an angle $d\theta$, increase of sensor area hit by the extra neutrons, will equal $2\pi r dr$. Assuming a function RD(r), that gives the radial distribution of scattering, the following equation can be stated:

$$F'(\theta)d\theta = \frac{1}{2} sin\theta d\theta = 2\pi r dr RD(r) \tag{42}$$

Using figure 25 and the small-angle approximation $sin(d\theta) \approx d\theta$, it can be seen that:

$$d\theta = \frac{D dr}{r^2 + D^2} \tag{43}$$

Combining equation (42) and (43) gives an expression for the radial distribution:

$$RD(r) = \frac{D}{4\pi (r^2 + D^2)^{\frac{3}{2}}} \tag{44}$$

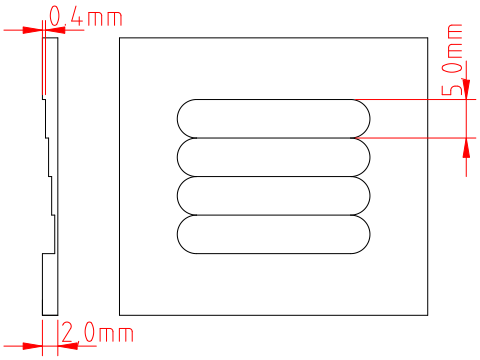

Figure 26: Technical drawing of the polyethylene plate used.

4.3.4 Uniform scattering correction

In this section the results of the final experiment are discussed, where a polyethylene plate is placed close in front of the sensor. In the plate, 4 lanes, 5mm wide, with an incremental thickness of 0.4mm were milled. In figure 26 a technical drawing of this polyethylene plate is shown. To correct for the blur due to scattering, uniform scattering, as discussed in the previous section, will be assumed.

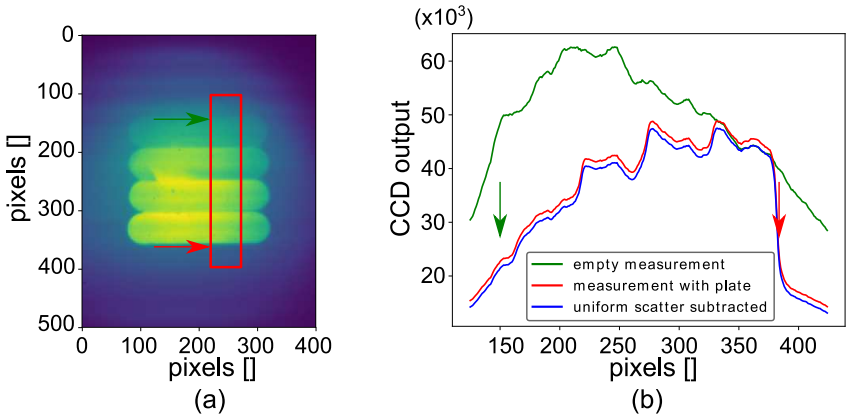

Figure 27: In figure (a) the CCD output is shown for the final experiment, where the red box shows the area that is averaged in the x-direction and shown in figure (b). In figure (b) the green line represents the incoming neutron bundle, the red line the CCD output and the blue line the CCD-output after being corrected for uniform scattering.

Figure 27a shows the processed CCD output for a measurement with the milled plate in front of the sensor. High CCD output corresponds to low thickness, hence the bottom lane has the smallest thickness. In figure 27b the CCD output is shown for a vertical

slab where for a given vertical pixel height the CCD-output is averaged over 10 pixels in the horizontal direction. As can be seen the CDD output of the measurement with a plate in front of the sensor becomes higher than the output of the empty measurement between 340-380 pixel height. This is a clear sign that scattering plays a significant role in this measurement, because the evident explanation for the higher intensity on that spot is that scattered neutrons will have caused the intensity to increase at that point. To correct for the contribution of scatter, the correction method as developed for this thesis and described in section 4.2 is applied and the uniform scatter distribution of the previous section is assumed. To calculate the normalization factor it is approximated that scattered neutrons only scatter once and that scattering is the only possible interaction, because of this approximation the normalization factor becomes:

$$NF_{i,j} = I^0_{i,j} - I^c_{i,j} \tag{45}$$

with NF the normalization factor, I^0 the intensity of the neutron bundle and I^c the calculated intensity with the polyethylene sample, which is the measured intensity subtracted by the scatter contribution

Basically a neutron now is assumed it can only have two states: it either did not interact with the polyethylene slap, which makes it part of I^c or it scattered once, which makes it part of NF. If it scattered, the probability it scattered on the sensor a distance r away from the position it would have hit the sensor if it didn‘t scatter is given by $RD(r)$. Now the function to be iterated becomes:

$$\begin{aligned} S_{i,j} \stackrel{?}{=} I^c_{i,j} + \sum_{k,l} NF_{k,l} * RD\left(\sqrt{(k-i)^2 + (l-j)^2}\right) * dA \\ = I^c_{i,j} + \sum_{k,l} \frac{(I^0_{k,l} - I^c_{k,l}) D dA}{4\pi((k-i)^2 + (l-j)^2 + D^2)^{\frac{3}{2}}} \end{aligned} \tag{46}$$

with S the measured intensity on the sensor, I^c the calculated intensity and dA the area size of a pixel.

In equation (46) I^c is updated after each iteration cycle until the 2 sides of the equation are equal. In figures 27b and 28 I^c is represented by the blue line and S by the red line. In figure 28a the ratio between the empty measurement and the measurement with the milled plate before and after scattering correction is shown. The 4 different lanes are visible and also it is clearly shown that the uniform scattering correction significantly changes the outcome. In figure 28b the ratio of figure 28a is converted to a thickness, using equation (5). In this figure the real thickness is indicated by the dotted black line. As can be seen the thickness is underestimated, So after subtracting the scatter contribution the intensity is still higher then expected, the most plausible explanation for this is that the scatter contribution is underestimated in the model. In figure 28b the result after subtracting a double amount of scattering is shown by the purple line. This represents a situation where all neutrons scatter uniformly but only in the forward half sphere. As can be seen, now the scattering is overestimated on the sides but still underestimated in the middle. Presumably this will change if not a uniform distribution

but a distribution where small scatter angles are more likely is being used. As can be seen multiplying the presumed scattering by 2 has a far greater effect on the total scattering than just a factor of 2, as in changing the assumed scattering has no linear effect on the final density field. This can be explained by the fact that when a greater amount of scattering on the sensor is assumed the amount of presumed unscattered neutrons will be lower. This causes on its turn that a greater fraction of neutron must have scattered and therefore further reduce the amount of presumed unscattered neutrons, etc. It is because of this effect that one can not just reverse the calculation and calculate the scatter angles from the result and known density field.

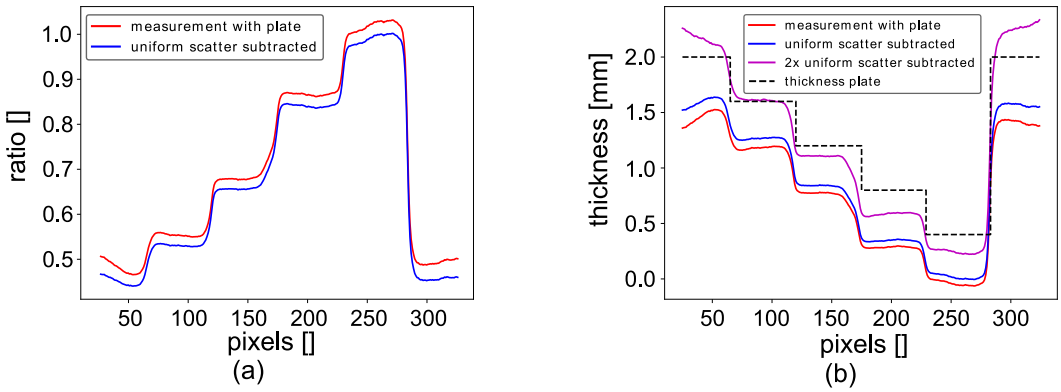

Figure 28: Ratio and thickness of sample before and after correcting for uniform scattering.

5 Recommendations for further research

In this section some recommendations are given for further research, with the objective of a working sensor that can measure the density of super critical water. Two main sources of uncertainty, sensor blur and scattering, are discussed.

5.1 Measuring sensor blur

In section 4.3 the existence of blur in the measurement due to uncertainties in the sensor is discussed. This blur increases the uncertainty of a measurement, especially in the case of a steep change in neutron intensity on the sensor. As shown in figure 22, the sharp edge of a pinhole is smeared out over a larger area. Correcting for this sensor blur could increase the accuracy of a measurement, but next to that, could also change the trade off made in the sensor design between capture efficiency and resolution. If the resolution can be enhanced computationally by correcting for the sensor blur, the scintillator plate thickness could be increased, causing a higher capture efficiency, which in turn would result in a lower measuring time.
In section 4.3.1 a potential correction method is evaluated to correct for the sensor blur using a function with two unknowns. It is reasonable to assume that a higher order polynomial will be a better representation for the radial distribution of the sensor blur. To find this higher order polynomial more constraints are needed. Using pinholes with different sizes will increase the amount of constraints by using equation (35). Alternatively instead of pinholes, slits of different sizes could also be used to increase the amount of constraints.

5.2 Measuring scattering

As shown in section 4.3.4, scattering contributes significantly to the uncertainty of a measurement. When the distribution of scatter angles is known, the blur due to scattering can be corrected. The difficulty lies in finding the distribution of scatter angles. An evident recommendation is to try to use Serpent or other neutron simulation software to calculate the radial distribution for a specific experimental case and see if this leads to better results. In case the simulation is not able to accurately calculate the distribution an alternative is to measure it. In this section proposals are discussed to measure this distribution more accurately.
In section 4.3.2 a pinhole was used in experiments, in order to measure the scatter angles. As shown in that section the blur induced by the sensor made it impossible to measure the scatter contribution. But also if the sensor blur could be corrected for or prevented, it is questionable if a usable result can be obtained. For a single pinhole, the scatter contribution to a specific pixel lays in the same order of magnitude as the noise measured in an empty or dark measurement. A more accurate way to measure the scatter contribution is to make use of symmetry. For example for a ring of neutron

scattering material, the middle of the ring has scatter contributions for only a limited range of scatter angles, depending on the thickness of the ring. Measuring the increase in neutron intensity in the centre, with a ring of neutron scattering material in place, will give a direct result for the amount of scattering at these angles. Different measurements with different ring sizes could together give a result for the distribution of scatter angles. As this distribution of scatter angles potentially depends on the kind of material being used, it is preferable to use the same material for testing as for the final measurements.

6 Conclusions

As shown in chapter 4.1 and figure 22 the neutron bundle used in this thesis shows some divergence. This causes an uncertainty in a measurement proportional to the distance between the sample and the sensor. In this thesis it is shown that putting the sensor directly behind the sample minimizes this uncertainty. However, putting the sensor close behind the sample does induce an uncertainty due to scattered neutrons that still hit the sensor. As shown in section 4.2 this uncertainty can be compensated for by an iterative algorithm if the probability function for the scatter angles is known. As shown in section 4.3 finding this probability function has been proven to be a challenging task. In section 5 a few ideas to improve the measurement of the probability function are proposed.
Looking at the main objective of this thesis: investigating the possibility of measuring the density profile of super-critical fluids with the use of neutron radiography, it can be concluded that, based on the results obtained in this work, this objective seems plausible. Although this thesis did not quantify the total uncertainty of a measurement, looking at the huge density differences of super critical water, measuring a clear trend in the density profile can be expected.

A Removing scatter blur example

In section 4.2 a method was introduced to remove the scatter blur from an image. In this appendix this process is explained on the basis of just 3 pixels. A measurement on a slab with the following densities is assumed:

0.3	0.4	0.5

When there is only absorption in the slabs and no scattering the neutron intensity can be easily calculated with the following equation:

$$I = I^0 e^{-\Sigma_x D} \tag{47}$$

Where I^0 is intensity of the incoming beam, Σ_x the macroscopic cross section, being dependent on the thickness and material of the slab and D the density.
If assumed that I^0 and Σ_x are both 1 in this fictitious example, the intensity on the sensor can be calculated. When equation (47) is reversed the density field can be reconstructed from the intensity:

density				intensity		
0.3	0.4	0.5	$\leftrightarrow$	0.74	0.67	0.61

If scattering is included, the calculation becomes a bit more difficult: To calculate the contribution of scattering to the intensity, one needs to know which fraction of the incoming neutrons is scattered and how these scattered neutrons are radially distributed. For this example a linear dependency is assumed for the scatter fraction, the normalization factor NF(D):

$$NF(D) = 0.05D + 0.1 \tag{48}$$

Since, in this example, only three pixels are used, the radial intensity distribution, RI(R), can only take two values, because there are only two distinct distances. The following values are assumed in this example:

$$RI(R) = \begin{cases} 0.25 \text{ for } R = 1 \\ 0.15 \text{ for } R = 2 \end{cases} \tag{49}$$

With the two formula‘s above, the intensity can be calculated with the effect of scattering taken into account, as also shown in equation (30):

$$S_{i,j} = I^0_{i,j} e^{-\Sigma_t(x) D_{i,j}} + \sum_{k,l} I^0_{k,l} * NF(D_{k,l}) * RI\left(\sqrt{(k-i)^2 + (l-j)^2}\right) \tag{50}$$

For example for the first pixel in our example this becomes:

$$I_1 = I^0_1 e^{-\Sigma_x D_1} + I^0_2 * NF(D_2) * RI(1) + I^0_3 * NF(D_3) * RI(2) \tag{51}$$

Doing this calculation for all pixels the following result can be obtained:

density				intensity		
0.3	0.4	0.5	→	0.868	0.820	0.719

Because the complete density field needs to be known for each point, it is not possible to directly reconstruct the density field from the intensity. It is possible, however, to iterate towards the correct answer. When, for example, the density is guessed to be the following:

density				intensity		
0.4	0.4	0.4	→	0.790	0.820	0.790

It can be seen that the intensity on the first pixel is lower and on the last pixel is higher than the previous result: so the density is overestimated in the first pixel and underestimated in the last. To update the density field equation (31) can be used:

$$D_{i,j}^{new} = D_{i,j}^{old} + (S_{i,j} - M_{i,j})/I_{i,j}^{0}\Sigma_t e^{-\Sigma_t D_{i,j}^{old}} \tag{52}$$

Which in this example means for the first pixel:

$$D_1^{new} = 0.4 + (0.790 - 0.868)/e^{-0.4} = 0.284 \tag{53}$$

Because only the direct effect of equation (47) was taken into account, the density change was overestimated a bit, but the new density field is much closer to the original value. This is because the direct effect has a much bigger influence. Iterating to the final result now gives:

density				intensity		
0.400	0.400	0.400	→	0.790	0.820	0.790
			↙			
0.284	0.400	0.506	→	0.881	0.819	0.714
			↙			
0.300	0.398	0.498	→	0.868	0.821	0.720
			↙			
0.300	0.400	0.500	→	0.868	0.820	0.719

As can be seen, the iteration converges quite rapidly.

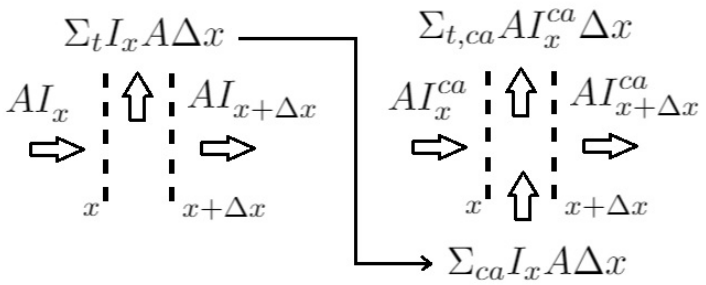

Figure 29: Schematic of the budget equation for neutron intensity.

B Fitting the normalization factor

In section 4.2 a method was introduced to remove the scatter blur from a measurement. One of the requirements for this method was a function for the normalization factor as a function of density. By measuring with a few known densities the normalization factor can be calculated for these densities and a fit can be made. This appendix will explain the analytical procedure of acquiring that fit.
Because equation 6 showed that changing the density has the same effect as changing the thickness, the following thought experiment will assume a different thickness instead of density:
Assumed is a very narrow bundle is going through a slab of material. The intensity of the bundle can be calculated by the following budget equation:

$$AI_x - AI_{x+\Delta x} = \Sigma_t I_x A\Delta x \tag{54}$$

Where A is the frontal area of the bundle.
Taking the limit of Δx to zero, the following differential equation can be obtained:

$$\frac{dI(x)}{dx} = -\Sigma_t I(x) \tag{55}$$

I is the intensity only of neutrons that did not interact with the slab.
If the intensity of the incoming neutron bundle is known this equation can be solved. As mentioned above the variable x, can be interchanged with the density. In that case only the value of Σ_t will change. The same balance can also be made for the intensity of the neutrons that have scattered but are still on a collision course with the sensor:

$$AI_x^{ca} - AI_{x+\Delta x}^{ca} = \Sigma_{t,ca} AI_x^{ca} \Delta x - \Sigma_{ca} I_x A\Delta x \tag{56}$$

Where I^{ca} is the intensity of scattered neutrons that will still hit the sensor, $\Sigma_{t,ca}$ the microscopic cross section for neutrons that are either absorbed or scattered to a course that will no longer hit the sensor and Σ_{ca} the microscopic cross sections for neutrons that scatter for the first time to an angle that still hits the sensor.

Similar to equation (54), equation (56) can also be rewritten to a differential equation when taking the limit of Δx to zero:

$$\frac{dI^{ca}(x)}{dx} = -\Sigma_{t,ca} I^{ca}(x) + \Sigma_{ca} e^{-\Sigma_t x} \tag{57}$$

For the above equation to hold it is assumed that the range of angles that a neutron can scatter to, to still hit the sensor, is not changing significantly between the front and the back of the slab. Furthermore it is also assumed that only a very small fraction of the neutrons scatter more than twice. Because the intensity of I^{ca} is 0 at x = 0 the equation above can be solved:

$$I^{ca}(x) = \frac{\Sigma_{ca}}{\Sigma_t - \Sigma_{t,ca}} \left(1 - e^{-(\Sigma_t - \Sigma_{t,ca})x}\right) e^{-\Sigma_{t,ca} x} \tag{58}$$

This equation is fitted in figure 30 with the blue line. The following values for the cross sections were fitted:

Σ_t	2.01146725
Σ_{ca}	1.23213268
$\Sigma_{t,ca}$	0.55130798

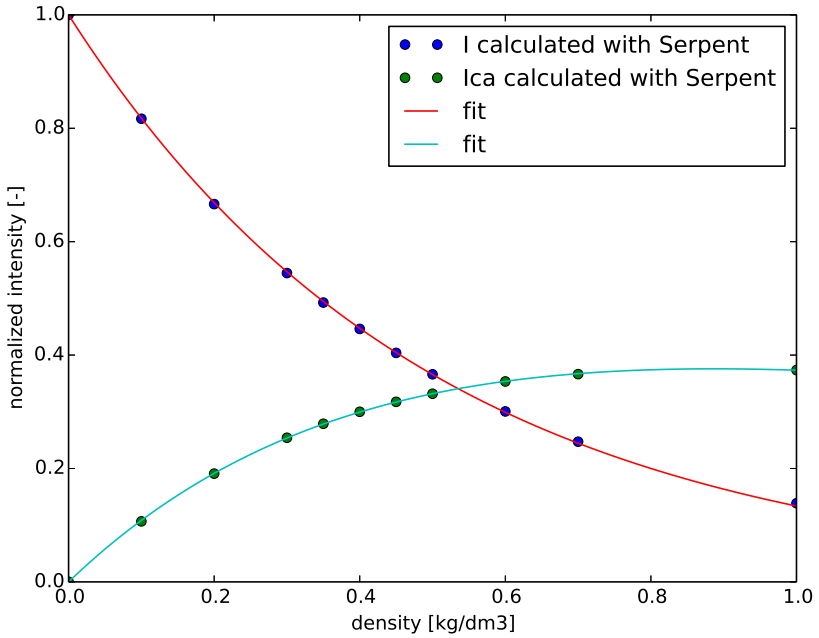

Figure 30: The intensities calculated with Serpent and their fits. The intensities are normalized with the strength of the incoming bundle.

References

[1] James J Duderstadt and Louis J. Hamilton, *NUCLEAR REACTOR ANALYSIS* university of Michigan, 1975

[2] Rahman et al, *Supercritical water heat transfer for nuclear reactor applications: A review* Annals of Nuclear Energy, volume 97, pages 53-65, 2016

[3] Strobl et al, *Advances in neutron radiography and tomography* Journal of Physics D: Applied Physics, volume 42, 2009

[4] Zboray et al, *In-depth analysis of high-speed, cold neutron imaging of air-water two phase ows* Flow Measurement and Instrumentation, volume 66, pages 182-189, 2019

[5] Hartnig et al, *Combined neutron radiography and locally resolved current density measurements of operating PEM fule cells* Journal of power sources, volume 176, pages 452-459, 2008

[6] Zhou et al, *FISH: A thermal neutron imaging station at HOR Delft.* Journal of Archaeological Science: Reports, volume 20, pages 369-373, 2018

[7] Zhou et al, *FISH: A thermal neutron imaging station at HOR Delft.* Journal of Archaeological Science: Reports, volume 20, pages 369-373, 2018

[8] K P Zetie et al *How does a Mach-Zehnder interferometer work?* Physics Education, Volume 35, 2000

[9] NASA website *https://www.grc.nasa.gov/www/k-12/airplane/tunvschlrn.html*

[10] Jeff database *https://www.oecd-nea.org/dbdata/nds_jefreports/jefreport-20/nea6287-jeff-20.pdf*

[11] Neutron Optics *http://www.neutronoptics.com/advantages.html*

[12] Neutron Irradiation facilities *https://www.tudelft.nl/en/faculty-of-applied-sciences/business/facilities/reactor-institute-delft/research-instruments/hoger-onderwijs-reactor-hor/neutron-irradiation-facilities/*

[13] Serpent *http://montecarlo.vtt.fi/index.htm*